Air Entrainment in High Pressure Multihole Gasoline Direct Injection Sprays

M. M. Khan[1,2,3†], J. Hélie[2], M. Gorokhovski[3] and N. A. Sheikh[1]

[1] *Department of Mechanical Engineering, Capital University of Science and Technology Islamabad, Pakistan*
[2] *Advanced System Engineering, Continental Automotive France, Toulouse, France*
[3] *Laboratoire de Mécanique des Fluides et d'Acoustique, CNRS – Ecole Centrale de Lyon INSA Université Claude Bernard Lyon, Ecully, France*

†*Corresponding Author Email: drmahabat@cust.edu.pk*

ABSTRACT

Experimental and numerical investigation of multihole gasoline direct injection (GDI) sprays at high injection pressure and temperature are performed. The primary objective of this study is to analyse the role of gas entrainment and spray plume interactions on the global spray parameters like spray tip penetration, spray angles and atomization. Three-hole 90° spray cone angle and six-hole 60° spray cone angle injectors are used for current work to examine the effect of the geometry of the injector on the spray interactions. The numerical results from Reynolds Average Navier Stokes (RANS) simulations show a reasonable comparison to experiments. The simulations provide further insight to the gas entrainment process highlights the fact that a stagnation plane is formed inside the spray cone which basically governs the semi collapse of spray that in turn affects the spray direction and cone angle.

1. INTRODUCTION

Typically multihole gasoline direct injection (GDI) injectors increase the quality of mixture formation and combustion in automotive engines. A GDI injector injects the fuel in form of multiple spray plumes at high pressure. The spray plumes at high injection pressure are well atomized. However optimal atomization alone cannot guarantee the best results. The spray plume angles, spray cone angles, direction of spray plumes and the penetration of the plumes are also equally important. These features of a GDI spray are governed by the interactions of spray plumes also called as jet-to-jet interactions. Jet-to jet interactions can produce highly unstable sprays which can lead to a partially or completely collapse of spray cone in certain cases. The air or gas entrainment process of GDI spray is mostly responsible for the jet-to-jet interactions. The global spray parameters like spray penetration, angles of sprays and the size of droplets in the sprays are investigated in (Befrui, *et al.* 2011). The role of vapor entrainment in mixture formation of GDI hollow cone spray is studied experimentally in Particle Image Velocimetry (PIV) (Prosperi, Helie et Bazile 2007). The influence of injection fluctuations on the variations of air entrainment in

sprays is also investigated using PIV in (Delay, *et al.* 2004). Air entrainment also affects the turbulent structures in the spray. One such investigation is carried out by (Seibel, *et al.* 2003) using for gasoline direct injection annular orifice spray. Another experimental study regarding multihole GDI injector highlights the fact that vapour accumulates inside the spray cone (Skogsberg, *et al.* 2005). However it fails to illustrate the reason of vapour accumulation and its effects on the behaviour of the GDI spray. A detailed experimental and numerical study of multihole GDI injectors are required to answer the open questions regarding the role of air entrainment in spray cone. Three different experimental setups are used to investigate different characteristics of the multihole sprays. Experimental investigation of the air entrainment is carried out by PIV technique. Mie-scattering imaging technique is used to capture the liquid phase of the spray plume. Phase Doppler Anemometry (PDA) is used to measure the droplet velocity and droplet sizes. Multihole injectors, particularly six hole injectors, produce extremely dense sprays. The interactions of spray plumes cause a substantial amount of laser scattering. Therefore the internal characteristics of spray cone become almost impossible to capture experimentally. That is why numerical simulations

are required to predict the properties of dense part of the spray.

2. EXPERIMENTAL SETUP AND OPERATING CONDITIONS

The measurement of GDI sprays are performed through two different experimental setups. The drop sizes and their velocities are measured by Phase Doppler Anemometry (PDA) and the measurement air entrainment of the sprays is accomplished by Particle Image Velocimetry (PIV). A brief description of both experimental setups is provided below.

2.1 PDA Test Bench

PDA is used to measure the drop sizes and their axial and radial velocities in GDI sprays. In current study, two component transmission system of PDA is preferred over single component system because the GDI sprays under high injection pressures produce dense sprays. Two laser beams of different wavelengths (in nanometers) are focused through various focusing lenses to produce two measurement volumes (in micrometers) for measuring axial and radial velocities. The drops that pass from the measurement volumes scatter the light that is collected by a receiver. Three-hole injector is used for PDA measurements since it is very difficult for the laser beams to pass through very dense sprays from six-hole injectors. The injector is rotated 360° in order to measure each spray at various radial positions. Similarly the laser beams are moved vertically in order to measure the drop velocities at different axial locations.

2.2 PIV Test Bench

PIV measurements are performed under high fuel pressure and high fuel temperature in a constant volume chamber. A cubical chamber with a total volume 1.4 Liter (112 mm x 112 mm x 112 mm) is used which can work at both high and low pressures (0-150 bar) and at high and low temperature (293-1000 K). The ambient pressure and temperature are controlled accurately. The fuel and injector nozzle temperatures are also controlled accurately using specific cooling and heating circuits. Each side of the chamber, except for the side where injector is mounted, provides an optical access for the imaging purpose.

Two gasoline direct injectors (GDI) are investigated that includes a three-hole 90° spray Cone Angle (CA) injector and a six-hole 60° CA injector. The injectors are tilted at 35° angle from z-axis to get a cross-sectional plane of measurement in between the two spray plumes. A two dimensional laser sheet is used as a source of light which is generated by systematic convergence and divergence of two laser beams. The laser sheet enters the chamber from the bottom window. The vertical alignment of the laser sheet is ensured by an angled mirror placed at the bottom of the chamber. Therefore the vertical measurement plane is illuminated by the laser sheet from bottom to top of the chamber.

2.3 Mie-Scattering Visualization Setup

The temporal liquid phase fuel distribution is captured by a high speed Mie-scattering setup. The liquid injected in the chamber is illuminated by halogen lamps. These lamps focus a continuous light on the spray that allows us to capture shadowgrapic images of the liquid spray with a help of high speed CCD camera.

2.4 Injector Design

The multihole injectors used in this study are three holes and six holes injectors. The cross-sectional view of the three holes injector is presented in the Fig. 1. The injector is equipped with a solenoid actuator which lifts the needle ball upon the supply of electrical signal. The pressurized liquid fuel is injected from the holes of the nozzle in form of spray. The Fig. 1 also shows different design parameters of one of the nozzle holes. The injection angle is denoted by β which is the half of the injector cone angle. The injection cone angle is measured from the central axis to center of the injection hole. The injection angle β for 3 holes injector is 38° and for 6 holes injector is 23°. The overall spray cone angle for three and six holes injectors are 90° and 60° respectively. The length of the injection hole is Li and Di is the diameter of the injection hole. The ratio of the length of the injection hole length to diameter of the injection hole is a key design parameter. As the larger value of Li/Di will lead to suppressed spray cavitation and smaller value of the ration will enhance the cavitation of the spray (Dahlander & Lindgren, 2009). The diameter and the length of the injection holes are 200μm therefore the ratio of Li to Di of 1 is used in GDI injectors. The ratio Li to Di for both three holes and six holes injectors is 1.1. The static mass flow rate (Qs) at 100 bar injection pressure with N-hyptane for 3 holes injector and 6 holes injector is 5.7 mg/ms and 11.4 mg/ms respectively. The mass flow rate profile is presented in Fig. 1 (b).
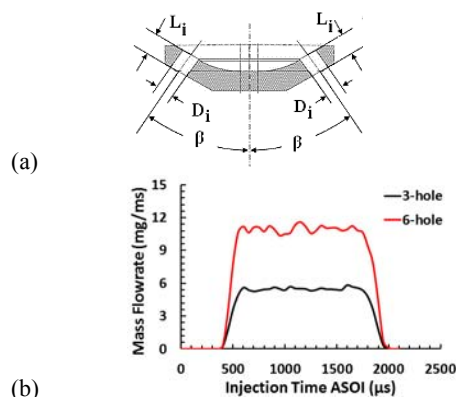

(a)

(b)

Fig. 1 (a) Injector design (b) Mass Flow rate profile.

2.5 Operating Conditions

The operating conditions are presented below in the Table 1.

Table 1 Operating conditions

Conditions	Experiments		
	1-PDA	2-PIV	3-PIV
Injector type	3 hole	3 hole	6 hole
Injection pressure	100 bar	200 bar	200 bar
Chamber Pressure	1 bar	1.54 bar	1.54 bar
Fuel Temperature	20 °C	90 °C	90 °C
Chamber Temp.	20 °C	33 °C	33°C
Injection duration	2 ms	3.32ms	3.387ms
Total inj. mass	15 mg	24 mg	48 mg
Fuel type	iso-octane	iso-octane	iso-octane

3. NUMERICAL MODELLING AND SIMULATION SETUP

OpenFOAM 1.7 is used to carry out numerical simulation of GDI sprays. Details of phase and spray modelling, computational mesh with boundary conditions are included in forthcoming sections along with description of numerical schemes used for simulations.

In general, a spray is a combination of liquid phase (droplets) and air/gas phase or the carrier phase. Being a two phase problem, both phases are treated differently. Carried phase is usually considered as Eulerian while droplets are modelled using Lagrangian technique.

3.1 Carrier Phase Modelling

The carrier phase is modelled using compressible Reynolds Averaged Navier-Stokes equations (RANS) approach.

$$\frac{\partial \rho}{\partial t} + \frac{\partial \rho \bar{u}_i}{\partial x_i} = \bar{S}_{mass} \qquad (1)$$

$$\frac{\partial \rho \bar{u}_i}{\partial t} + \frac{\partial \rho \bar{u}_i \bar{u}_j}{\partial x_j} = \frac{\partial \bar{p}}{\partial x_i} + \frac{\partial (\bar{\sigma}_{ij} + \tau_{ij})}{\partial x_j} + \bar{S}_m \qquad (2)$$

$$\frac{\partial \rho \bar{e}}{\partial t} + \frac{\partial \rho \bar{e} \bar{u}_j}{\partial x_j} = -\frac{\partial \bar{p} \bar{u}_j}{\partial x_i} + \frac{\partial \bar{u}_j (\bar{\sigma}_{ij} + \tau_{ij})}{\partial x_j} + \bar{S}_e \qquad (3)$$

The terms with overhead bars represent ensemble averages. While the source terms for mass, momentum and energy balances are given by S_{mass}, S_m and S_e respectively. ρ represents the carrier phase density; and pressure is denoted by p. Indices i and j stands for the coordinate directions and the three dimensional stress tensor $\bar{\sigma}_{ij}$, which includes eddy viscosity terms, is modelled using K-Epsilon model (Launder and Spalding 1972).

3.2 Liquid Phase Modelling

Lagrangian method for the droplets mainly relies on Newton's law of motion. For spherical drops the resultant form of the liquid phase is given by (Maxey et Riley 1983),

$$\frac{1}{6} \rho_p \pi d_p^3 \frac{d\mathbf{u}_p}{dt} = \frac{1}{2} (\mathbf{u}_g - \mathbf{u}_p) |\mathbf{u}_g - \mathbf{u}_p| \rho_g C_D \frac{\pi d_p^2}{4} \qquad (4)$$

The density of droplets is represented by ρ_p and the their size is denoted by d_p. All body forces are neglected while the drag force coefficient is represented by C_D. While the velocities of drops and gas phase are denoted by $\mathbf{u}_p$ and $\mathbf{u}_g$ respectively. It can be shown that above relationship reduced to Stokes drag by,

$$\frac{d\mathbf{u}_p}{dt} = \frac{C_D}{\tau_p} (\mathbf{u}_g - \mathbf{u}_p) \qquad (5)$$

Reynolds number of the droplet is denoted by Re_p whereas τ_p is the droplet relaxation time.

$$Re_p = \frac{|\mathbf{u}_g - \mathbf{u}_p| d_p}{\nu_g}, \quad \tau_p = \frac{4}{3} \frac{\rho_d d_p}{\rho_g C_D |\mathbf{u}_p - \mathbf{u}_g|} \qquad (6)$$

$$C_D = \begin{cases} 24/Re_p & Re_p < 0.1 \\ \dfrac{24\left(1 + \frac{1}{6} Re_p^{2/3}\right)}{Re_p} & 0.1 < Re_p < 1000 \\ 0.424 & Re_p > 1000 \end{cases} \qquad (7)$$

3.3 Spray Modelling

Pressurized liquid jet ejected to quasi-static gaseous environments experience sudden breakup to smaller droplets. This cluster of small droplets moving at high velocity in a continuum is also referred as Spray (Khan 2014). Moreover, for high pressure fuel injections, injecting blobs are preferred which requires only a secondary atomization model for description. With the spray plume moving downstream after dissociation, its anatomy become more and more subtle due to enhance effects of drag, intra-droplet collisions, evaporation and related phenomenon. Amongst the prominent features, air entrainment rate is one of the most influential parameter affecting the motion of droplets. To effectively model such spray several sub-models are required and OpenFOAM provides a variety of sub-models which are included in this work.

3.3.1 Drop Size Distribution Model

The probability density function for the liquid fuel injection, in the form of drop parcels with finite diameters, follows Rosin Rammler distribution (Khan 2014).

$$pdf = d_{po} + d_p \left(-ln(1 - N_{rand} K_R)\right)^{-q} \qquad (8)$$

where $K_R = 1 - exp\left[(d_{pm} - d_{po})^q / \langle d_p \rangle\right]$, d_{po} stands for the minimum while d_{pm} is the maximum diameter sizes for the mean diameter $\langle d_p \rangle$. N_{rand} is the random number used for the distribution. The spread of the drop distribution is attributed to the spreading factor q estimated from the experimental data.

3.3.2 Secondary Atomization Model

Secondary atomization of drops occurs at high weber numbers due to their oscillation leading to distortion resulting in their break up. Using Enhanced Taylor Analogy, secondary breakup can be modelled with

spring, mass and damper analogy. Surface tension is analogue of the spring force while the fluid viscosity acts as the damper (Tanner 1997). While following relationship governs the rate of new droplet production (Tanner 1997).

$$\frac{d\bar{m}(t)}{dt} = -3K_{br}\bar{m}(t) \tag{9}$$

This ensures that the ratio of child droplets size (d_{child}) to its parent's size (d_{parent}) is $e^{-K_{br}t}$. The value of K_{br} varies depending on droplets breakup regime and their oscillation frequency (w),

$$K_{br} = \begin{cases} k_1 w & We \leq We_{cr} \\ k_2 w \sqrt{We} & We > We_{cr} \end{cases} \tag{10}$$

where k_1 and k_2 are the constants. Droplet breakup regime relies on the value of Weber number (We), ratio of inertial to the surface tension forces. Using experimental observations, critical Weber number (We_{cr}) is identified. At lower values We bag breakup regime is expected, therefore the value for We_{cr} is set at 80. Above We_{cr} stripping breakup regime is expected to take place. The two regimes observe different characteristics of breakup. Bag breakup is seen when the droplet forms a bag like shape before bursting while droplets tend to flatten and form sheet like shapes with stripping at the edges identify the stripping breakup regime.

3.3.3 Droplet Collision Model

Droplet collisions are modelled using Nordin Trajectory model (Nordin 2001) which is a modified O'Rourke collision model (O'Rourke 1989). The original form of O'Rourke model does not cater for the parcel directions, while trajectory model accounts for the intersection points for the parcel before the collision. Using the orientation velocity vector, it ensures that the droplets are travelling towards each other leading to collision

$$\mathbf{u}_{align} = \left(\mathbf{u}_{p2} - \mathbf{u}_{p1}\right) \frac{(x_{p2} - x_{p1})}{|x_{p2} - x_{p1}|} \tag{11}$$

The velocities of the interacting droplets are denoted by $\mathbf{u}_{p1}$ and $\mathbf{u}_{p2}$ with their respective locations as x_{p1} and x_{p2}. In case if droplets are destined for collision then their collision distance is calculated using their velocities and the simulation time step (Δt)

$$\mathbf{u}_{align}\Delta t > |x_2 - x_1| - 0.5(d_{p2} - d_{p1}) \tag{12}$$

In case if the parcels approach collision radius within a time step then the collision takes place, otherwise the trajectories are revaluated at the next time step.

3.3.4 Droplet Dispersion Model

The carrier phase disperses the droplets through turbulent eddies. For droplet dispersion a stochastic dispersion model is employed which relies on turbulent kinetic energy and dissipation (Dukowitz 1980). The dispersion model calculates the time spent (T_{drop}) by the droplet to pass through the eddy. Then using the turbulent flow properties (turbulent kinetic energy k & turbulence dissipation (ε) the time taken for a single turn by an eddy (T_{eddy}) is estimated,

$$T_{eddy} = \min\left(\frac{k}{\varepsilon}, c_{ps} \frac{k^{\frac{3}{2}}}{\varepsilon} \frac{1}{|\bar{\mathbf{u}} + \mathbf{u}'|}\right) \tag{13}$$

c_{ps} is a constant while the average carrier fluid velocity at the droplet's location is denoted by $\bar{\mathbf{u}}$. The fluctuating component at the same location is shown by $\mathbf{u}'$.

The droplet remains unperturbed by the eddy motion in case $T_{drop} < T_{eddy}$. However, if $T_{drop} > T_{eddy}$ then droplet is assigned a new direction in random fashion.

3.3.5 Droplet Evaporation and Heat Transfer Model

D^2-law (Godsave 1953, Spalding 1953) is employed to model droplet evaporation using evaporation relaxation time (τ_e) and evaporation coefficient (C_e).

$$d_{p_i}{}^2 = \tau_e C_e \tag{14}$$

Ce is function of Sherwood number (Sh) which is calculated using Frössling correlation (Crowe, Sommerfeld et Tsuji 1998).

Nusselt number (Nu), used for calculation evaporation relaxation time, is estimated using heat transfer model of Ranz-Marshal (Ranz et Marshall 1952)

$$Nu = 2 + 0.6 \, Re_p{}^{1/2} Pr^{1/3} \tag{15}$$

It is pertinent to mention that for the numerical simulations presented here the standard evaporation along with above mentioned heat transfer model are perceived to work well. It is also important to note that for the flash boiling conditions, the flashing effects are incorporated in the injection model i.e. reduced drop size and increased spray angles. Therefore, the modelled spray is primarily highly evaporating spray.

3.4 Numerical Schemes

The simulation approach used combination of reacting spray solver suitable for compressible flows (based on standard dieselFoam) and automatic mesh refinement (AMR) of interDyMFoam. The AMR enabled solver is implemented in OpenFOAM ® (Kosters 2010). PISO (pressure implicit with splitting off operators) (Demirdžić, Lilek et Perić 1993) is used with two iterations for predictor correction.

The numerical schemes used for this work are second order accurate for space discretisation and first order accurate for time discretisation. For the divergence operators, Gauss limited linear scheme which is a bounded scheme of second order is utilized. Gauss linear corrected scheme which is unbounded conservative scheme of second order is applied. First order accurate Euler Implicit scheme was used for stability as it depends on the courant number. In order to keep courant number less than 0.5 automatic time stepping is implemented with initial time step
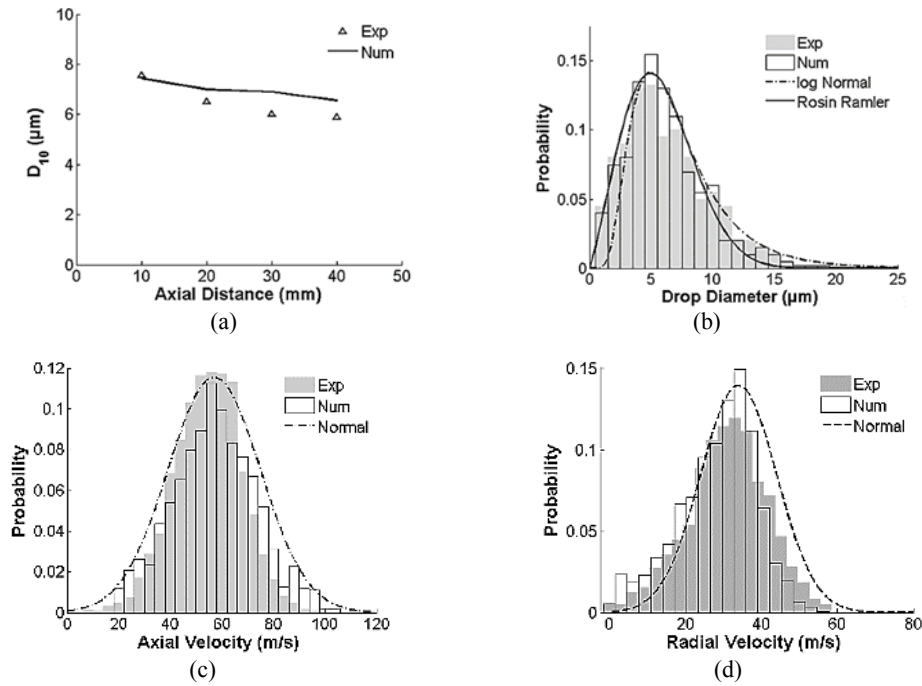
Fig. 2 Experimental and simulation results of 3-hole injector; (a) Mean droplet diameter (D_{10}) at different axial locations, (b) PDF of droplet distribution at 40 mm axial location (c) PDF of droplet axial velocity at 40 mm axial location (d) PDF of droplet radial velocity at 40 mm axial location.

size of 10^{-7} sec. Solver used for pressure equation was based on Preconditioned bi-conjugate gradient method (Hestens et Stiefel 1952) with Diagonal incomplete-Cholesky (symmetric) while Diagonal incomplete-LU (asymmetric) was used for velocity, kinetic energy and other terms with minimum residue of 10^{-7} at each time step.

3.5 Computational Domain

The computational domain is a cubical of 112mm each side is used with an initial cell size of 1.5mm. Mesh refinement was carried out at an interval of 2 with a maximum limit of 5.0 million number of cells. This led to a minimum cell size of 0.375mm after two refinements. Maximum limit ensures that the maximum number of cells does not cross computational limits. AMR is linked with scalar field variable such as kinetic energy and vapour mass fraction of non-evaporating and evaporating conditions respectively.

4.   RESULTS AND DISCUSSION

The results are discussed below for both non-evaporating and evaporating conditions in detail.

4.1 Non Evaporating Cases

Table 1 summarizes the comparison of experimental PDA data with simulation results of droplet size distribution for a 3-hole injectors under non-evaporating conditions. Fig. 2 (a) compares the numerical predictions of average droplets size (D10) with the experimental results at different axial locations along the center of plumes during 1.6 - 2ms

time interval. At 10mm downstream along the center of plume, experimental results for mean droplet size of 7.55μm matches reasonably well with numerical predictions of 7.43μm. The experimental mean droplet size reduces to 5.89μm at 40mm compared to 6.55 μm predicted by numerical results (see Fig. 2 (b)). 40mm downstream along the center of a single separated plume, the droplet size distribution Probability Density Function (pdf) also shows a good agreement. For comparison two standard particle distributions, log normal (Eq. 16) and Rosin Rammler (Eq. 17) distributions, are also used.

$$pdf = \frac{1}{d_p S_{td} (2\pi)^{0.5}} e^{-\left[\frac{(ln(d_p)-M_n)^2}{2S_{td}^2}\right]} \qquad (16)$$

The two tuning factors namely M_n and S_{td} are mean and standard deviations adjusted to empirically fit the data. Here $M_n = 1.85$ and $S_{td} = 0.5$ respectively.

$$pdf = q\langle d_p \rangle^{-q} d_p^{q-1} e^{-\left(\frac{d_p}{\langle d_p \rangle}\right)^q} \qquad (17)$$

Rosin Rammler distribution uses different values for the mean diameter ($\langle d_p \rangle = 6.5$) with spread factor (q = 2.2).

It can be noted that both distribution functions show reasonable fitting with experimental as well as numerical data. One may note that almost all larger droplets are well captured by the Log normal distribution function, however it misses smaller drops. While small drops are well captured by the Rosin Rammler profile but on the contrary it fails to fit some of the larger drops. Despite their

imperfections, both distributions are quite useful in comparison of drop size distribution at various locations. Near the injection region, with the probability of larger drops, Log normal distribution function is expected to work better while further away in downstream direction, Rosin Rammler distribution can be employed due to smaller droplet sizes.

The experimental and numerical distribution of axial and radial droplets velocities at 10mm downstream position are compared in Fig. 2 (c) and (d) respectively. The distribution of the axial and radial velocity is normally distributed. The numerical results are comparable to the experimental results.

4.2 Non Evaporating Cases

4.2.1 Axial liquid Spray Penetration

Along the direction of flow, spray axial liquid penetration rates are compared for both 3-hole as well as 6-hole injectors. The evaporating conditions are listed in Table 1. The comparison of experimental and simulation results in Fig. 3 show that despite their nominal geometrical differences both 3-hole and 6-hole injectors have similar penetration rates. The comparison of numerical results with experimental data show good match. Initial delay of 400 μs was observed in the experimental data, for both 6-hole and 3-hole injectors, due to physical delay between the injector trigger (electrical signal) and the actual start of injection i.e., advent of liquid at the nozzle exit. Solenoid activation delay as well as hydraulic delay (nozzle internal flow) both contribute towards this delay, therefore the delay is also included in the numerical simulations so that the comparison shows both results at same starting time of fuel injection. The delay in simulation is incorporated through the mass flow rate profile as presented in Fig. 1 (b).
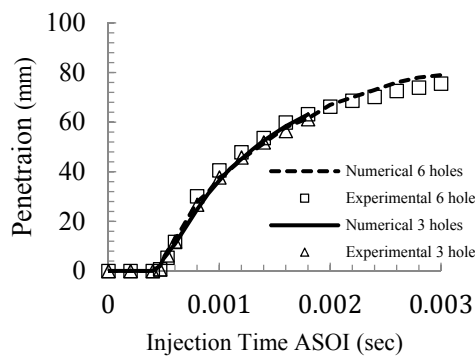

Fig. 3. Comparison of penetration curves under evaporating conditions for 3 and 6-hole injectors.

4.2.2 Air entrainment in Spray Plumes

Numerical and experimental comparisons of the air entrainment in the highly evaporating spray plumes injected from 3-hole and 6-hole injectors are presented in Fig. 4. Two dimensional vertical cross-sections which bisect the two spray plumes are considered for this purpose. The spray from 3-hole injector is

Under the evaporating conditions, 2D flow fields' comparisons are presented for measured experimental and simulated numerical results. Characteristics of the air entrainment for the 3-hole in Fig. 4 (a & b) and 6-hole injectors Fig. 4 (c & d) are presented, at time instant of 1.75 ms After Start Of Injection (ASOI). For both injectors, the numerical results show reasonable agreement with the experimental data. It can be noticed that in the region near the nozzle exit, air velocity is high due to high spray momentum compared to the leading edge of spray.

On the other hand, 6-hole injector reveals a significantly different flow physics. Experimental data suggests that the spray collapses. It is presumed that this collapse is linked with the jet-jet interactions and this is likely to influence the air entrainment characteristics. Due to sudden collapse of spray it is not possible to collected PIV data in the inter-jet spacing for the 6-hole injector, therefore, the resulting formation only appears to have a continuous spray plume. For the sake of comparison the air entrainment data between the jets from the simulation has not been included at this point but it will be discussed later in detail. The difference between the numerical and experimental results for both injectors are presented in Fig. 4 (e & f). It can be noticed from the magnitude and direction of error vectors that the maximum difference does not exceed 2.5m/s and mostly appears locally or linked with the flow directions instead of its magnitude.

4.2.3 Interaction of Spray Plumes

As mentioned earlier, jet to jet interactions can be important for multi-hole injectors which can influence the general spray structure. For the 6-hole injector, simulation results under the evaporating conditions reveal the presence of significant jet-jet interactions. This appears to modify the trajectory of the individual spray plumes as shown in Fig. 5. For the 3-hole injector the spray plumes appear to be well separated. On the other hand, the 6-hole injector reveals a semi collapsing spray structure. The dense spray plumes and narrow configuration of the six hole injector makes it quite hard to recognise individual plumes. This suggests that the adjacent plumes/jets interact significantly and thus modify the air entrainment characteristics and inadvertently influence the air-fuel mixture distribution. Due to limitations of experimental technique such flow aspects can be studied in more detail by performing numerical simulations.

4.2.4 Spatial Evolution of Vapor Phase

Numerical simulations provide further insight of the processes leading to flow physics characteristics especially for 6-hole injector under evaporating conditions. Using sequence of vapour phase imaging at various cross sections downstream of the spray injection reveals the propagation, structure and mixture formation of the spray. For instance, at 3.10ms ASOI Fig. 6 shows the vapour mass fractions along the axial direction of the spray plumes. A star-shaped spray plume structure is evident very near the
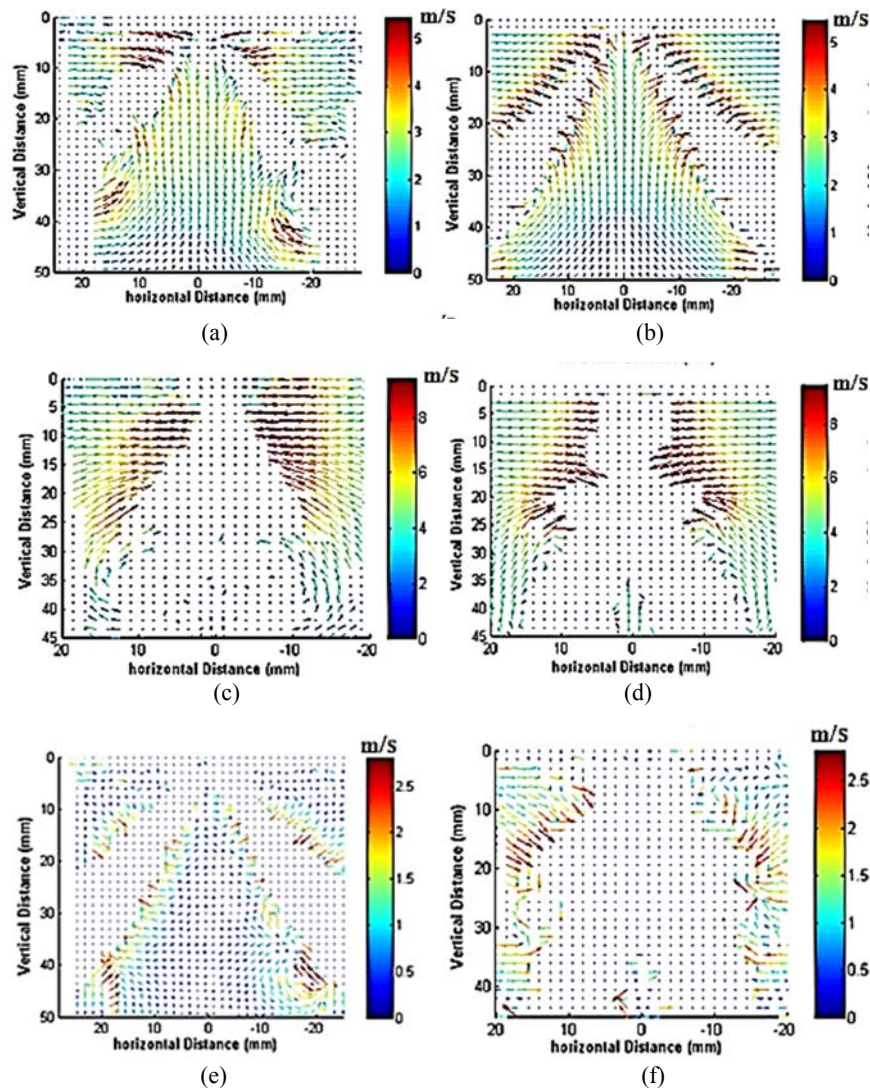
Fig. 4. 2D vector flow fields showing air entrainment at 1.4ms ASOI for the 3-hole injector (a) Experimental, (b) Simulation; for the 6-hole injector (c) Experimental, (d) Simulation; Error between experiment and simulation for (e) 3-hole (f) 6-hole.
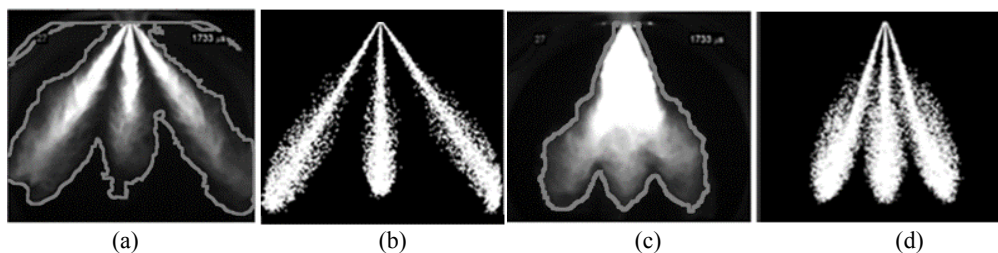

Fig. 5. Liquid phase spray images of the sprays under evaporating conditions at 1.75ms ASOI; (a) Experimental result (high-speed Mie scattering) of 3-hole injector (b) Simulation result of 3-hole injector (c) experimental result (high-speed Mie scattering) of 6-hole injector (d) Simulation result of 6-hole injector.

nozzle exit with each plume revealing own structure separated from neighbouring plumes.

The images also reveal that the fuel vapours lie towards the central region of spray. Moving away from the nozzle, downstream the vapours of fuel begin to merge in to one another as revealed by the close-ring like structure instead of earlier star-shaped formation. The resultant structure of the spray resembles that of a hollow cone (Rottenkolber, *et al*. 2002). At this stage the trajectories of the spray
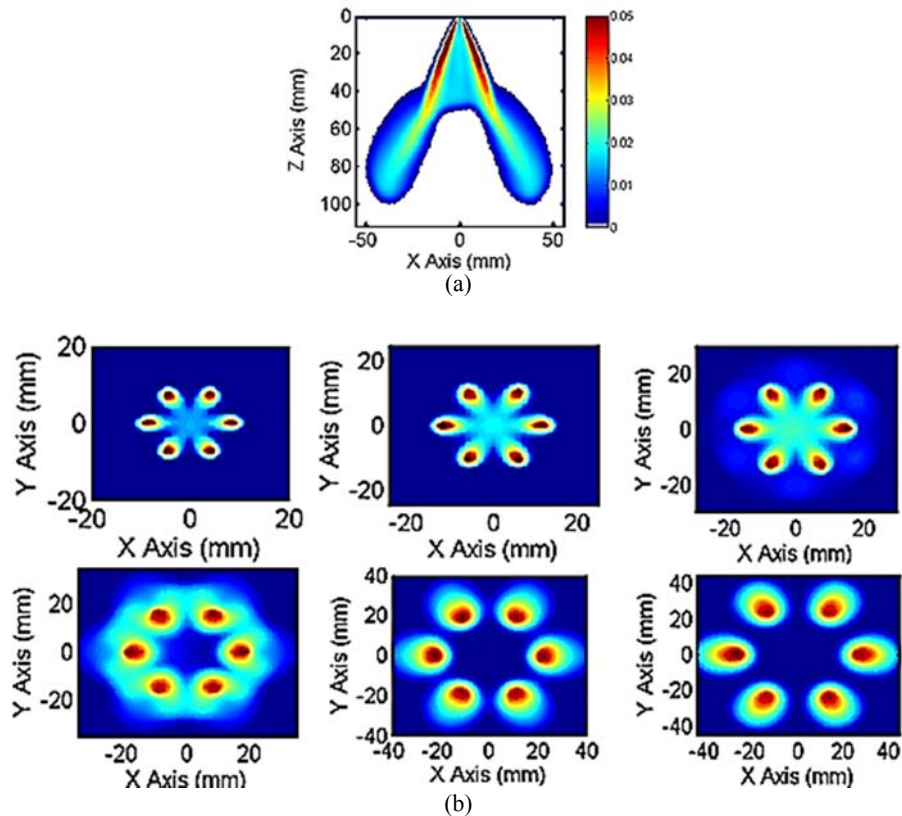
Fig. 6. Numerical fuel vapor mass fraction at time 3.1ms ASOI, (a) 2-D axial cross-sectional plane (x, z); (b) 2-D horizontal cross-sectional planes (x, y) with (top left) 20mm, (top middle) 30mm, (top right) 40mm, (bottom left) 50mm, (bottom middle) 60mm, (bottom left) 70mm.
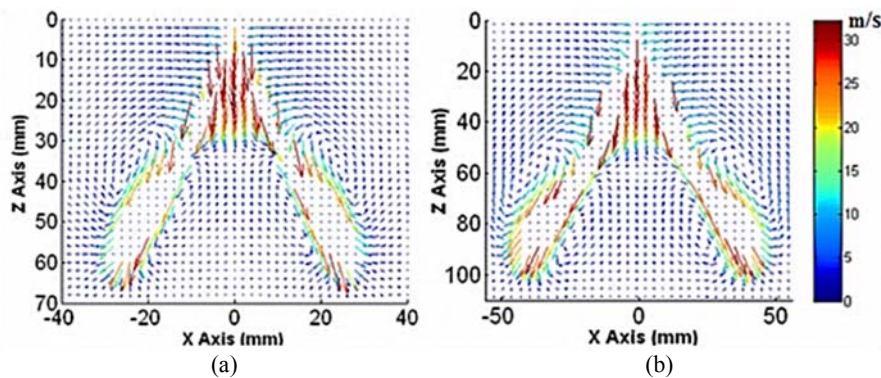

Fig. 7. Two dimensional velocity vector plots of simulated air and gas entrainment; (a) 1.75ms ASOI, (b) 3.10 ms ASOI.

plumes tend to deflect and a notable change is evident in spray angle. The process takes place as the spray propagates and could be better explained if the air entrainment characteristics are analysed.

4.2.5 Axial Gas Velocity

The vertical cross section (x-z plane) of air entrainment between two adjacent spray plumes from a 6-hole injector at 1.75ms and 3.10 ms ASOI are shown in Fig. 7. In general, air entrainment in the spray plumes can be divided in to two regimes; (1) in the region closer to the nozzle exit air is drawn in and (2) the air and vapor mixture is pushed downstream

towards the spray tip (Prosperi, Helie et Bazile 2007) and (Skogsberg, *et al*. 2005). Both of these two regimes can be observed here as towards the nozzle exit vapor is being drawn inwards in first phase and forced downwards towards the spray tip as shown in Fig. 7.

Further to above, a new characteristic of spray is revealed related to air flow between the two adjacent jets. Air between the two jets is pushed downstream in the upper half of the spray cone. This is contrary to the well separated jet streams and wide cone angle sprays such as 3-hole injector as shown in Fig. 7.

The resultant downward flow of gas, in the upper zone of the spray cone, encounters a flow in the opposite direction which originates from the bottom half of the spray cone usually known as internal air entrainment. The two oppositely moving stream interact at 30mm at 1.75ms and 50mm at 3.10ms, a stagnation plane is formed which produces radial flow towards the periphery of the spray as seen in Fig. 7. This strong radial flux causes the spray plume to deflect suddenly from its original trajectory and a significant change in angle can be noted. In the current operational conditions, the collapsing tendency vanishes at this location and the plumes are separated from each other which can also be seen in Fig. 6.

While a second difference in the bottom half of the spray cone can be observed in 6-hole injector compared to 3-hole injector. In this region the spray tip recirculations on the internal side are comparatively weaker than the outer spray tip recirculations. This causes asymmetric external/internal flow as observed in the region where the jet plumes are widely separated.

4.2.6 Comparison of Spray Angles

High speed Mie-imaging is used to capture the spray angles of six hole injector and compared to simulated results as presented in Fig. 8. As discussed previously, the spray cone can be segregated in two zones, one close to the nozzle and second in the downstream region where a modification of the spray cone angle is evident. Through images the corresponding cone angles are measured in the y-z plane. Corresponding to 1.75 and 3.10 ms ASOI, the spray cone angles are analyzed using Matlab. The far plume angle in both experiments and simulation presented in Table 2 show a good agreement. The far plume angle in experiments (α_{fe}) is found to be 61º and the fr plume angle in simulation (α_{fs}) is calculated to be 62 º on both instances.
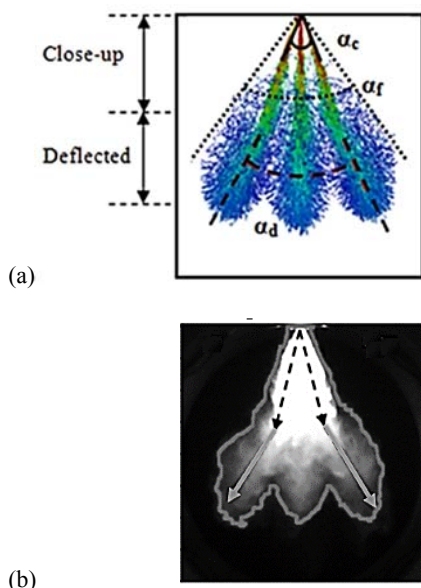
Table 2 Angles of close-up and deflected part of the 6-hole spray at time 1.75 ms and 3.10 ms

Angles	Time (ASOI)	
	1.75 ms	3.10 ms
Overall Close-up cone angle from Simulation	54º	54º
Overall Deflected cone angle from Simulation	60°	61°
Far cone angle from Simulation (α_{fs})	62°	62°
Far cone angle from Experiment (α_{fe})	61°	61°

However spray cone angle measurement in the first zone (near nozzle) (α_c) is approximately 42°. It should be noted that αc is measured from center of the spray plumes on both sides. Therefore with an addition of half spray plume angles on both sides of the spray cone gives an overall spray close-up cone in the upper zone of the spray cone of 54°. Spray angles near the nozzle region suggest that the measured cone angle is narrower than its prescribed value of 60°. The difference of approximately 6° from the prescribed angle suggests that the near nozzle region has a spray collapse in the upper region.

Towards the downstream of spray, the overall deflected spray cone angle of approximately 60°, at 1.75 ms ASOI, is measured which increases to 61° at 3.10 ms ASOI. This suggests that the spray cone angles in the downstream zone are similar to the prescribed cone angles but the direction of the spray plume is different from the intended direction of the spray plumes as observed in Fig. 8 (b).

Therefore a very important conclusion can be drawn from these results. The spray far cone angles shows a remarkably good comparison between the experimental and numerical results, however the spray plumes appear to propagate with two different angles in the injector close up and in different directions in the far zones. Which indicates that that overall spray cone angle is not an absolute indicator of spray direction especially when strong jet-jet interactions take place. Therefore the angle between α_c and α_d should be used as an indicator of the spray direction.

4.2.7 Radial Gas Velocity

Figure 9 shows the radial velocity vectors in horizontal directions of the air entrainment at various axial locations at time of 3.10 ms. It can be noticed that the till 40mm downstream of the spray, air is being sucked in from the outer region. Afterwards the air along with vapor is pushed out from the center of the spray cone. Inner side of the plumes, the air entrainment is caused by the accelerating flows between the adjacent jets. Some of the air is trapped between these jets, which cannot turn due to high momentum flux and is pushed further downstream. As described earlier, in the spray core region air is moving in opposite directions at 40mm and 60 mm

(a)

(b)

Fig. 8. 2D Comparison of spray plumes at 1.8 ms ASOI; (a) Simulation result (b), experimental result.
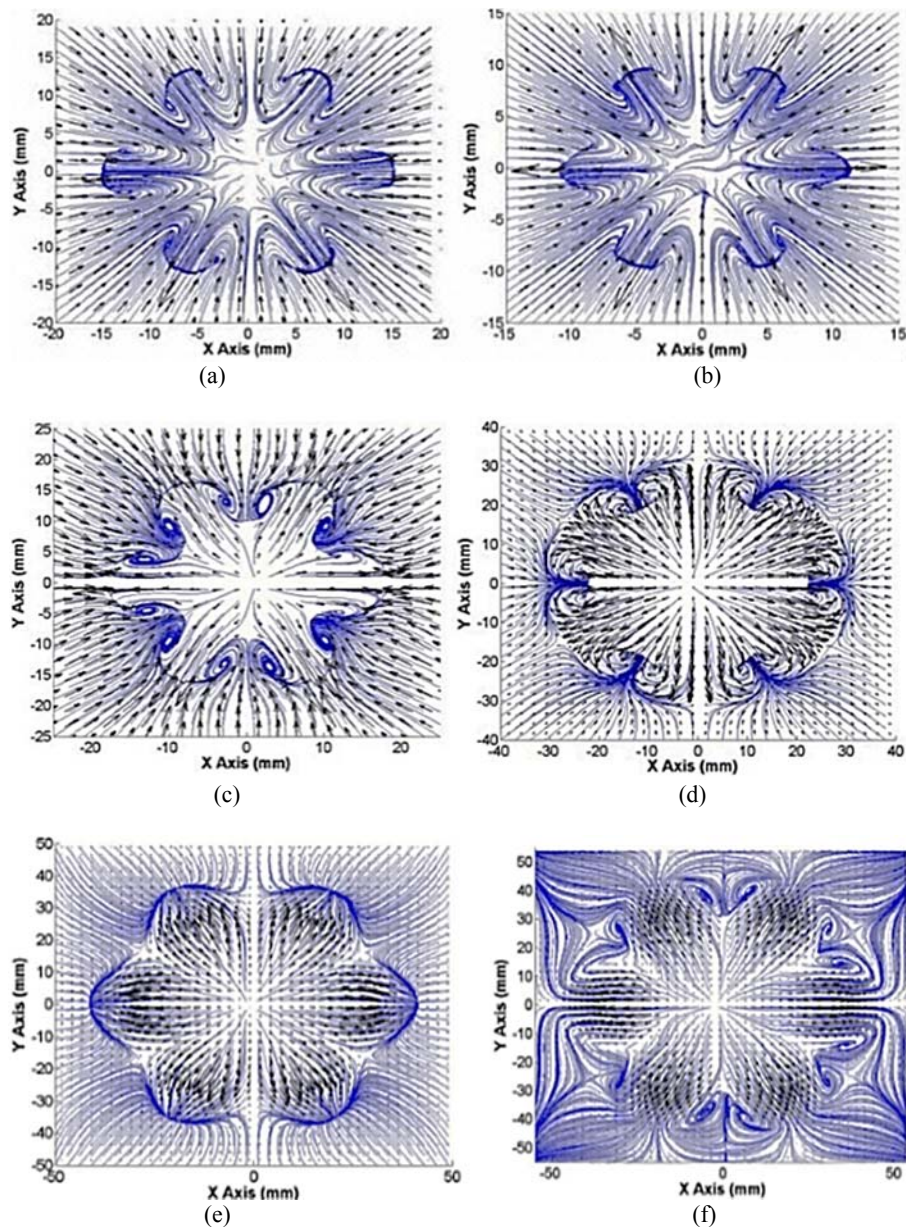
Fig. 9. Radial velocity vector plot of the simulated air entrainments at 3.10ms ASOI at downstream locations; (a) 20mm (b) 30mm (c) 40mm (d) 50mm (e), 60mm (f), 70mm.

and as the air vapor mixture is pressed downwards while the air is drawn upwards, both streams hit each other and form a stagnation plan. At this point strong radial flow is been generated which causes the spray to bend.

This is evident in the Fig. 9 (d) at 50 mm downstream. One may observe a ring of gas pushing outwards; this is produced by the interactions of opposite gas velocity in the core of spray cone. The presence of strong radial flow as presented in Fig. 9 (d) is relatively larger than the air entrainment from outside the spray cone. The strong radial flow blocks the outer region air from the spray cone and leads the spray plumes to bend from their original path.

Further downstream, at 70mm, the observed radial

velocity is primarily a projection of the air entrained in the spray with accompanying large external recirculation around the jets. This indicates the position where the process of jet-to-jet interaction is almost finished and the jets propagates linked to its previous (bent) direction.

4.2.7 Flux Balance

As discussed earlier the flux of air that enters the spray cone could not be immediately entrained. Therefore it is highly imperative to identify the percentage of air that is not entrained by the spray plumes. For this purpose air flux balance is calculated around the stagnation plane. A control volume is used, 5mm apart in axial direction, to compute the flux that enters the spray cone and the

flux that leaves the spray cone without being entrained. The stagnation plane travels in axial direction in time. Therefore the flux is calculated by moving the control volume axially at various positions at 1.35ms ASOI. It is observed in Fig. 10 that the amount of flux that cannot be entrained by the spray plumes increase systematically from the near nozzle region to the point where the stagnation plane is present. It shows that almost 60% of the flux cannot be entrained by the spray plumes. After the stagnation plane most of the flux is entrained by the spray plumes
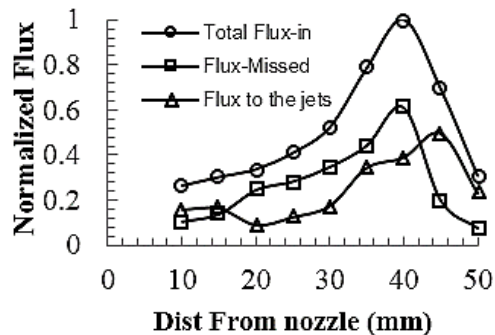

Fig. 10. Axial air entrainment flux.

5. CONCLUSION

The spray properties of multihole gasoline direct injectors are investigated under non-evaporating and evaporating conditions. The experimental and numerical comparison of spray characteristics under non-evaporating and evaporating conditions show good agreement. Numerical simulations capture liquid penetration, droplets sizes and velocities reasonably well. The standard spray models with adaptive mesh refinement also showed good agreement with PDA and PIV results.

Simulations provide additional information regarding the jet to jet interactions and partial spray collapse in case of six hole injector. Six hole injector produces narrow angled spray cone. The interactions of the spray jets are strongly linked to compact geometry of six hole injector. High momentum of the spray jets and narrow spray cone result in pushing the entrained air downwards. This process is continuous and it prevents the spray cone expansion. The air entrainment flux from the bottom half of the spray cone eventually interacts with entrainment flux from top half and forms a stagnation plane. The stagnation plane produces a radial force that bends the spray plumes. The vapor from the center of the spray plumes is pushed outwards and a ring like structure is formed. Therefore the spray cone under strong jet to jet interactions lead to a collapsing zone (upper zone) of the spray cone and a downstream zone with deflected spray plumes. The spray cone angles in upper and downstream zone are very different. Therefore the spray cone angle cannot be considered as the true indicator of spray plumes direction. The direction of the spray plumes should be based on the angles of collapsing spray cone

portion and deflected portion.

The spray plume direction and penetration play crucial role in the performance of GDI injectors. Based on the results, the spray cone angle, distance between the injection holes and the injection opening velocities are identified as the three most important controlling parameters. Larger spray cone angles and larger distance between the injection holes minimize the spray plume interaction. Higher injection opening velocity increases the spray momentum in the vicinity of the nozzle and thus reduces spray plume interactions and spray collapse.

REFERENCES

Befrui, B, G. Corbinelli, M. D. Onofrio and D. Varble (2011). GDI Multi-Hole Injector Internal Flow and Spray Analysis. *SAE Technical Paper.*

Crowe, C., M. Sommerfeld and Y. Tsuji (1998). *Multiphase Flows with Droplets and Particles.* CRC Press LLC.

Delay, G., R. Bazile, G. Charnay and H. Nuglisch (2004). Temporal dependency of air entrainment to liquid flow rate variations for gazoline direct injection sprays. In: Temporal dependency of air of laser tecniques to fluid mechanics. *International Symposia on Applications of Laser Techniques to Fluid Mechanics.* Lisbon.

Demirdžić, I., Ž. Lilek and M. Perić (1993). A collocated finite volume method for predicting flows at all speeds. *International Journal for Numerical Methods in Fluids* 16, 1029-1050.

Dukowitz, J. K. (1980). A particle-fluid numerical model for liquid sprays. *Journal of Computational Physics* 35, 229.

Godsave, G. A. E. (1953). Studies of the combustion of drops in a fuel spray—the burning of single drops of fuel. *Symposium (International) on Combustion.* Elsevier. 818-830.

Hestens, M. R. and E Stiefel. (1952). Methods of Conjugate Gradients for Solving Linear Systems. *Journal Research National Bureau of Standards* 49, 409-436.

Khan, M. M. (2014). *RANS and LES of multi-hole sprays for the mixture formation in piston engines.* Lyon, France: Doctoral dissertation, Ecole Centrale de Lyon.

Kosters, A. (2010). *Dynamic mesh refinement in dieselFoam.* CFD with OpenSource software, project report, Division of Combustion, Chalmers University of Technology.

Launder, B. E. and D. B. Spalding (1972). *Lectures in Mathematical Models of Turbulence.* London, England: Academic Press.

Maxey, M. R. and J. J. Riley (1983). Equation of motion for a small rigid sphere in a nonuniform flow. *Physics of fluids A* 26, 883-889.

Nordin, N. (2001). Complex chemistry modeling of diesel spray combustion. PhD thesis, Dept. of Thermo and Fluid Dynamics, Chalmers University of Technology, Göteborg.

O'Rourke, P. J. (1989). Statistical properties and numerical implementation of a model for droplet dispersion in a tur bulent gas. *Journal of Computational Physics* 83, 345–360.

Prosperi, B, J. Helie and R Bazile. (2007). PIV measurements of injection pressure effect on gas entrainment in GDI engines. Turkey: ILASS Europe.

Ranz, W. E. and W. R. Marshall (1952). Evaporation from drops. *Chem. Eng. Prog* 48, 141-146.

Seibel, C., K. Gartung, S. Arndt and B. Weigand. (2003). Detailed analysis of spray structure and air entrainment in GDI sprays using a tomographic approach. *ICLASS.* Sorrento.

Skogsberg, M., P. Dahlander, R. Lindgren and I. Denbratt (2005). Effects of Injector Parameters on Mixture Formation for Multi-Hole Nozzles in A Spray-Guided Gasoline DI Engine. *SAE.*

Spalding, D. B. (1953). The combustion of liquid fuels. *In Proceedings of the Fourth Symposium (International) on Combustion.* Elsvier. 847-864.

Tanner, F. (1997). Liquid Jet Atomization and Droplet Breakup Modeling of Non-Evaporating Diesel Fuel Sprays. *SAE Technical Paper* 970050.